Geophys. J. Int. (2007) **169,** 1028–1042 doi: 10.1111/j.1365-246X.2006.03319.x

Imaging the deep structure of the San Andreas Fault south of Hollister with joint analysis of fault zone head and direct *P* arrivals

M. A Lewis,[1] Y. Ben-Zion[1] and J. J. McGuire[2]

[1]*Department of Earth Sciences, University of Southern California, Los Angeles,* CA 90089-0740*, USA. E-mail: malewis@usc.edu*
[2]*Department of Geology and Geophysics, Woods Hole Oceanographic Institution, Woods Hole,* MA 02543*, USA*

Accepted 2006 December 4. Received 2006 November 30; in original form 2006 February 16

SUMMARY

We perform a joint inversion of arrival time data generated by direct *P* and fault zone (FZ) head waves in the San Andreas Fault south of Hollister, CA, to obtain a high-resolution local velocity structure. The incorporation of head waves allows us to obtain a sharp image of the overall velocity contrast across the fault as a function of depth, while the use of near-fault data allows us to resolve internal variations in the FZ structure. The data consist of over 9800 direct *P* and over 2700 head wave arrival times from 450 events at up to 54 stations of a dense temporary seismic array and the permanent northern California seismic network in the area. One set of inversions is performed upon the whole data set, and five inversion sets are performed on various data subsets in an effort to resolve details of the FZ structure. The results imply a strong contrast of *P*-wave velocities across the fault of ∼50 per cent in the shallow section, and lower contrasts of 10–20 per cent below 3 km, with the southwest being the side with faster velocities. The presence of a shallow low velocity zone around the fault, which could corresponds to the damage structures imaged in trapped wave studies, is detected by inversions using subsets of the data made up of only stations close to the fault. The faster southwest side of the fault shows the development of a shallow low velocity FZ layer in inversions using instruments closer and closer to the fault (<5 and <2 km). Such a feature is not present in results of inversions using only stations at greater distances from the fault. On the slower northeast side of the fault, the presence of a low velocity shallow layer is only detected in the inversions using the stations within 2 km of the fault. We interpret this asymmetry across the fault as a possible indication of a preferred propagation direction of earthquake ruptures in the region. Using events from different portions of the fault, the head wave inversions also resolve small-scale features of the fault visible in the surface geology and relocated seismicity.

Key words: fault models, head waves, interfaces, low-velocity zone, seismic velocities, tomography.

1 INTRODUCTION

1.1 Fault zone structure and head waves

Understanding the structure of large faults is an important step towards the understanding of earthquake processes on those faults. Various studies have made use of closely spaced networks of seismometers to produce tomographic images of the crustal seismic velocities around large continental faults (e.g. Eberhart-Phillips & Michael 1993; Scott *et al.* 1994; Thurber *et al.* 1997). However, direct *P*- or *S*-wave arrival time tomography cannot resolve well the short length scales that are important for earthquake physics, and the same holds for reflection/refraction studies in the case of near-vertical faults. This is because (1) the arrival time picks of *P* and *S* body waves are not sensitive to low velocity zones, and (2) the traveltime is a function of the entire source–receiver path, of which a narrow fault zone (FZ) structure would be a very small part. These methods are thus inadequate for revealing details of the localized FZ structure at depth.

A number of studies have suggested that FZ trapped waves can be used to obtain a high resolution image of the seismogenic structure of specific fault segments (e.g. Li *et al.* 1990; Li *et al.* 1997b). FZ trapped waves result from the constructive interference of critically reflected phases within a sufficiently uniform zone of low velocity (damaged rock) that acts as a waveguide (Ben-Zion & Aki 1990; Igel *et al.* 1997). As a result, the characteristics of observed FZ trapped waves depend strongly on the average geometry and seismic properties of the generating low velocity layer (Ben-Zion 1998; Jahnke *et al.* 2002). In the last 15 yr, trapped waves were used to image FZ layers with width of 10s to a few 100s of metres in the structure of several large fault and rupture zones. These include the San Andreas fault (SAF) near Parkfield (Li *et al.* 1991; Li *et al.*

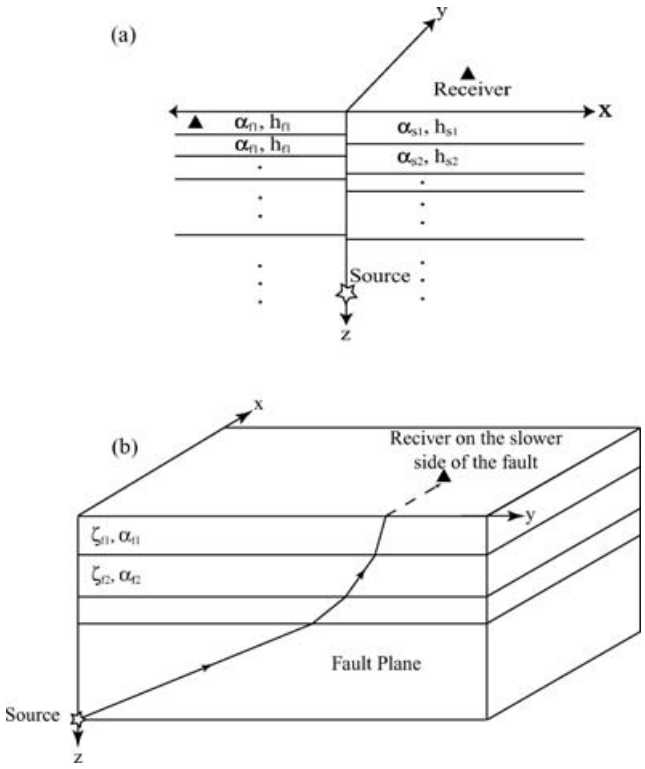

Figure 1. (a) Cross-section perpendicular to the fault showing the structure of the layered quarter spaces fault zone velocity model. The *P*-wave velocities and layer thickness are denoted by α and h, respectively, with subscripts fj and sj representing the fast and slow sides of the fault for each layer. The source (star) is on the fault at depth and the receivers (triangles) are located in the *x*–*y* plane on the surface or at some depth *z*, less than the thickness h1 of the shallowest layer. (b) A view in the direction perpendicular to the fault, showing the ray path (arrows) of the head wave along the fault plane, which is the coordinate used for the head wave traveltime calculation. The vertical components of rays and *P*-wave velocities in layer j on the faster side of the fault are denoted by ζ_{fj} and α_{fj}, respectively. From Ben-Zion *et al.* (1992).

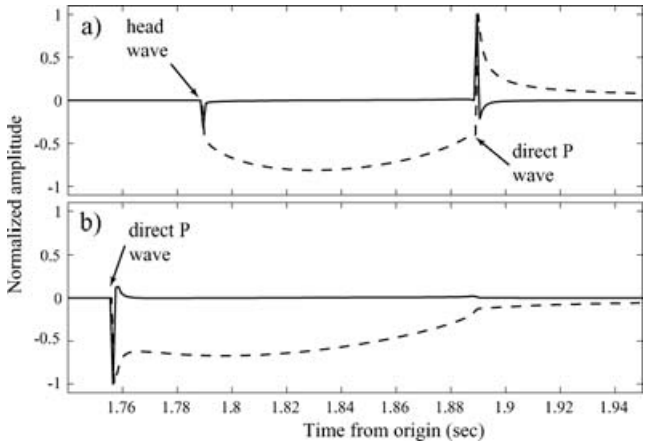

Figure 2. Synthetic seismograms based on the 2-D analytical solution of Ben-Zion (1989) for a line dislocation with a unit step function in time at the interface between two quarter-spaces with different materials properties. The contrast of *P*-wave velocities between the two quarter-spaces is set at 25 per cent. (a) Normalized velocity (solid) and displacement (dashed) seismograms for an instrument 10 km along and 2 km normal to the fault on the quarter-space with slower velocity. The motion at this position consists of a first arriving emergent head wave followed by a sharp direct *P* arrival. (b) Same as (a) but for a receiver 2 km normal to the fault on the quarter-space with faster velocity. The motion at this position consists only of a direct *P* arrival.

1997a; Michael & Ben-Zion 1998; Korneev *et al.* 2003), the San Jacinto fault near Anza (Li *et al.* 1997b; Lewis *et al.* 2005), an inactive fault in central Italy (Marra *et al.* 2000; Rovelli *et al.* 2002), the Landers rupture zone (Li *et al.* 1994; Peng *et al.* 2003) and the Karadere-Duzce branch of the North Anatolian fault (Ben-Zion *et al.* 2003). The modelling of trapped waves is, however, associated with large trade-offs between key FZ parameters (Ben-Zion 1998). For example, considerably different propagation distances within the FZ can fit the same waveforms equally well if appropriate changes in the FZ width, velocity and attenuation coefficients are made. As a result, robust conclusions based on waveform modelling of FZ trapped waves, without constraining evidence on some of the parameters, are very hard to draw. Furthermore, a growing body of evidence based on comprehensive multisignal analysis of large data sets suggests that the damage zones producing trapped waves are generally limited to the upper ∼3–4 km (Rovelli *et al.* 2002; Ben-Zion *et al.* 2003; Korneev *et al.* 2003; Peng *et al.* 2003; Lewis *et al.* 2005). It thus appears that trapped wave studies cannot provide detailed information on the fault structure at seimogenic depths, except that it is not characterized by a uniform damage zone extending continuously from the surface.

Plate boundaries and other major faults may juxtapose rock bodies with different elastic properties. Two regions where juxtaposition of different crustal blocks has been imaged using seismic tomography are the Cienega Valley area (Thurber *et al.* 1997) and Parkfield section (Eberhart-Phillips & Michael 1993) of the SAF, with the contrast of seismic velocities extending throughout the seismogenic zone. A sharp material contrast separating different crustal blocks will generate (Ben-Zion 1989; Ben-Zion 1990; Ben-Zion & Aki 1990) fault zone head waves (FZHW) that spend a large portion of their propagation paths refracting along the material interface that defines the fault (Fig. 1). The head waves propagate along the material interface with the velocity and motion polarity of the faster block, and are radiated from the fault to the slower velocity block where they are characterized (Fig. 2) by an emergent waveform with opposite motion polarity to that of the direct body waves. The FZHW are the first arriving seismic energy at locations on the slower side of the fault with normal distance to the fault (Ben-Zion 1989) less than a critical distance x_c

$$x_c = r \bullet \tan\left[\cos^{-1}\left(\frac{\alpha_2}{\alpha_1}\right)\right], \quad (1)$$

where r is the along-fault propagation distance and α_2 and α_1 are the average *P*-wave velocities of the slower and faster media, respectively.

The existence of material interfaces in FZ structures can have important implications for many aspects of earthquake physics, including effective constitutive laws, suppression of branching, frictional heat, short rise-time of earthquake slip, earthquake interaction and seismic shaking hazard (Ben-Zion & Andrews 1998; Ben-Zion 2001). Since the FZHW are generated by and travel along material interfaces, they provide the best diagnostic and imaging tool of material contrasts at seismogenic depths of faults. Ben-Zion & Malin (1991) and Ben-Zion *et al.* (1992) identified FZHW along the Parkfield section of the SAF and inverted arrival time data of the FZ head and direct *P* waves for the local velocity structure. Ben-Zion *et al.* (1992) also performed numerical experiments showing that the use of head waves can significantly improve the resolution of the velocity structure across the fault. More recently, McGuire & Ben-Zion

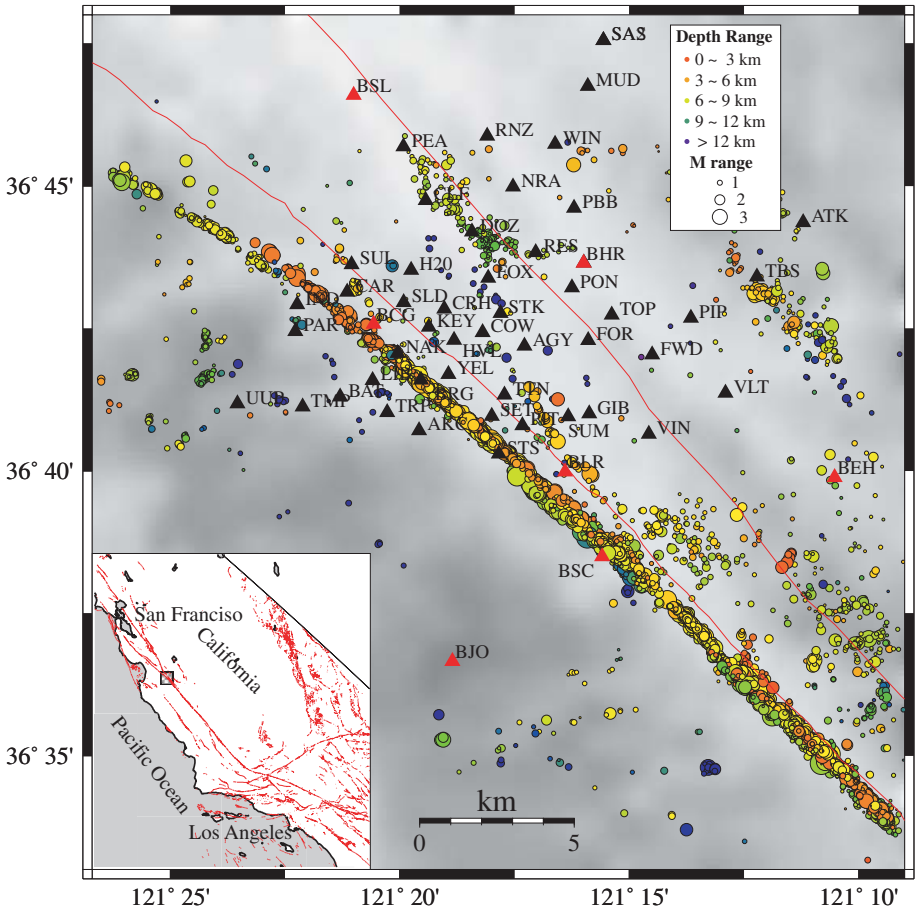

Figure 3. A map of the study area with grey shading used to represent topography and red lines the surface traces of significant faults. The black triangles represent stations in the temporary array while the red triangles are permanent station from the NCSN, all of which labelled with their three letter code names. The circles are positions of 12 yr of events relocated by McGuire & Ben-Zion (2005). The size of each circle scales with the event magnitude and the colours represent their depth. The inset on the bottom left shows a large scale map, with major faults marked in red, major cities, and the location of the main map inside a small box.

(2005) analysed arrival times and waveforms characteristics of FZHW, direct *P* waves and additional FZ phases in the early portion of seismograms, using data collected from a dense temporary array (Thurber *et al.* 1997) around the SAF south of Hollister. The results demonstrated clearly the existence of pronounced material interfaces, sufficiently planer and sharp to generate head waves, in the seismogenic structure of the SAF in that area.

In the present work, we derive additional information on the fine velocity structure of the SAF south of Hollister, based on joint inversions of FZHW and direct *P* arrival times. The inversions employ a simple model geared to focus on the arrival times of seismic phases generated in a layered structure with a sharp planar material interface. Using this model with different station and earthquake combinations allows some exploration of how the structure varies along strike and with distance from the fault. As shown in the following sections, the employed simple model and a related complementary framework can explain well the major features (arrival time, amplitude and polarity) of the seismic phases in the early portions of the observed seismograms While a fully 3-D model would be required to explain all the observed features, our focus is on imaging the velocity structure in the immediate vicinity of the SAF. This narrow structural component can be imaged well by analysis of the observed near-fault *P* phases and FZ head waves within the simplified framework of our model.

1.2 Data and geological setting

The Cienega Valley to Bear Valley region of the SAF south of Hollister lies at the northern end of the creeping section (Fig. 3) and is characterized at the surface by granites plus Pliocene and Cretaceous sediments (Thurber *et al.* 1997). The SAF is generally the interface between the higher velocity igneous rocks to the SW and lower velocity sedimentary rocks to the NE. Thurber *et al.* (1997) deployed a 48-station PASSCAL array around the SAF (Fig. 3), with the aim of performing local *P*-wave arrival time tomography. The instruments were a mix of standard short period seismometers, primarily Mark products L22s, L4s and Teledyne S-13s, with 33 located on the NE side between ∼200 m and as much as 10 km away from the surface trace of the fault. In the 6 months that the temporary array was deployed, some 1200 local events were recorded and have locations in the Northern California Seismic network (NCSN) catalogue. With instruments positioned closely around the fault on both the fast SW and slow NE sides, and with a clear velocity contrast across the fault, the deployment is well suited for FZHW analysis.

In the present work, we analyse data recorded by Thurber *et al.* (1997) and additional seven permanent NCSN stations in the study area. We use accurate earthquake locations from McGuire & Ben-Zion (2005) based on the double difference technique (Waldhauser & Ellsworth 2000) when available, and otherwise the standard

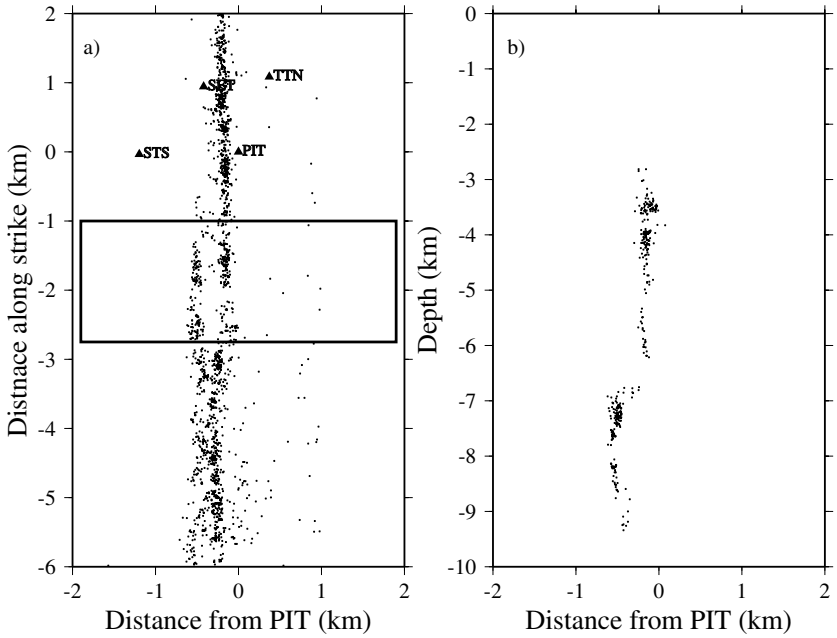

Figure 4. Relocated earthquakes in the region of the structural complexity. (a) A map view of the earthquakes, black dots, and the southeasterly stations of the network, triangles, rotated to have the fault running straight from top to bottom and on a local coordinate system centred on station PIT. The box denotes an area, shown in cross-section in (b), where the fault splits into two branches. (b) The events from the box in (a) plotted onto a vertical plane. The two fault branches can be seen to be active in different depth ranges.

NCSN catalogue locations from the Northern California Earthquake Data Center. The relocated events generally collapse onto an approximately 100–200 m wide near-vertical zone that is offset to the SW from the surface trace of the fault. There is a long standing debate on whether this offset is produced by the velocity contrast across the fault (e.g. Bakun *et al.* 1980; Ellsworth 1975), or whether it reflects a fault dip (e.g. Aki & Lee 1976; Thurber *et al.* 1997). To reconcile the narrow near-vertical zone containing the relative locations of the relocated seismicity and the surface trace of the fault, we follow McGuire & Ben-Zion (2005) and shift the double-difference locations 0.7 km to the NE. This distance is chosen so that the seismicity is 100–200 m to the SW of station PIT, a location consistent with the surface trace of the fault. This shift is also necessary to produce first motion polarities and frequency contents consistent with right lateral focal mechanisms on a near-vertical fault at stations on the southwest side near the fault.

The offset between the surface trace and the inferred event locations is not consistently 0.7 km throughout the area but rather increases to the NW. Nevertheless, the seismicity in our analysis is approximated as a plane with the assumed fault model consistent with the average locations, after they are shifted 0.7 km to the NE. We note that the uncertainty in the absolute locations normal to the fault has a small effect on our results, which are based on arrival time data that are sensitive primarily to the distance travelled along the fault. As discussed in Section 2.2, sets of inversions in which the assumed fault position is varied within a zone of 1000 m show that the resulting change to the obtained velocity contrast is only about 1 per cent (which is less than the variations between inversion runs in the same set).

To the southeast of the network the relocated hypocentres do not collapse onto a single plane, but to a pair of parallel strands that are active in different depth ranges (Fig. 4). The strands are also shown in the geological map of the area (Dibblee 1974), with the surface trace of the SAF splitting into two branches separated by a sliver of granitic rocks. The double-strand structure also manifests itself in the waveforms of events with origins to the south of the temporary network, with at least one extra phase between the head and direct wave arrivals. When performing waveform modelling, McGuire & Ben-Zion (2005) found that the energy between the head and direct waves (Fig. 5b) requires an intermediate velocity layer, consistent with a sliver of granite, between two quarter spaces with different elastic properties. This structure impinges our study in two main ways. First, picking the arrival times of the phases, particularly the direct wave, for events to the SE of the network is less accurate. Second, the model that we use for the arrival time inversions (Fig. 1) consists of two layered quarter-spaces separated by a single interface. Thus data generated by events on both the parallel strands are mapped by our ray tracing model to a single effective interface, rather than being fully accounted for. As discussed above, small changes of locations normal to the fault have little impact on our results.

Taking into account the structural complexity to the southeast, it would be preferable to concentrate on performing inversions for the part of the SAF within and to the NW of the network. However in the period of operation of the dense temporary array, only about 120 (10 per cent) of the events occur on the simple (single-trace) portion of the fault. Of the 300 events for which arrival times have been picked on instruments of the temporary array, more than 50 per cent come from within, or to the SE of, the section of the fault with the double-strand structure. Results based on such data would, therefore, be skewed towards this area where our model simplifies an important structural component. To work with a more balanced data set that averages small-scale complexities not accounted for by the model, 150 events that occurred before the operation of the array to the north of the double-strand area and were recorded by the seven NCSN stations are also used. This gives an approximately even distribution of the number of arrival times from the regions of the fault within and to the NW and SE of the dense temporary

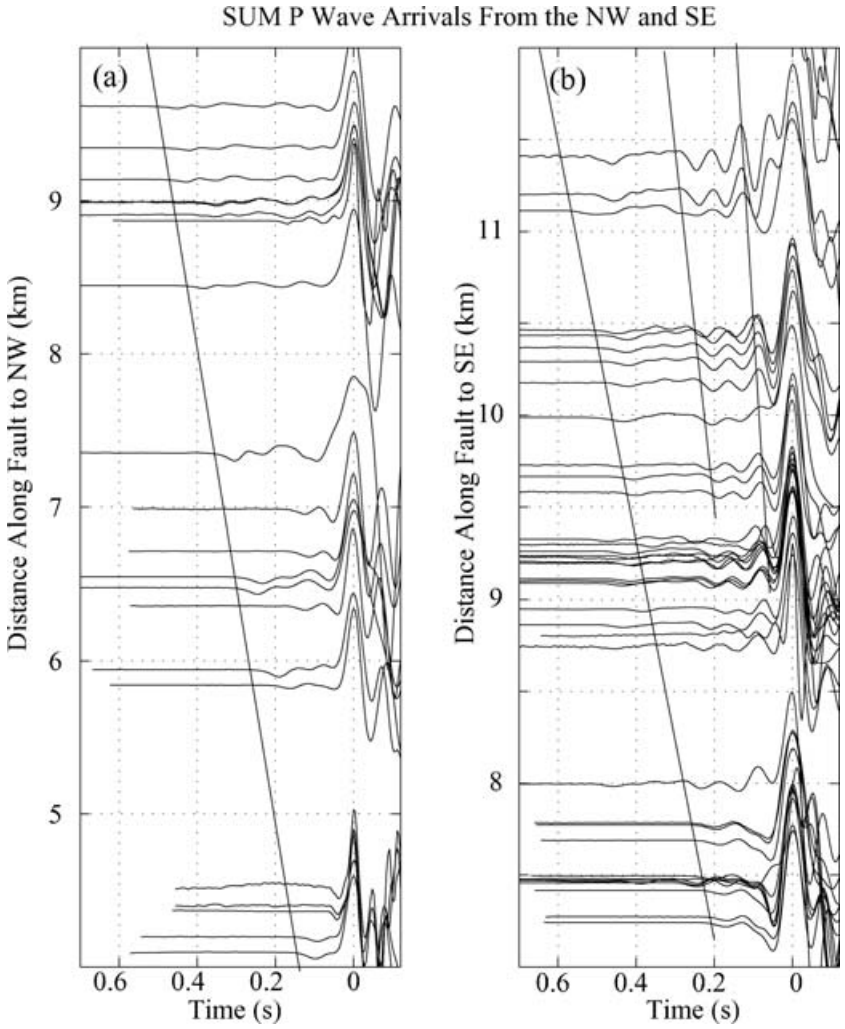

Figure 5. Vertical component velocity seismograms recorded at station SUM and aligned on their *P* waves arrival plotted at the distance of that event along strike from the station. (a) Seismograms of events to the northwest of the station with the head wave arrivals delineated by a black line. A clear moveout between the direct *P* and head waves as the distance travelled increases can be seen. (b) Seismograms of events to the southwest of the station showing additional complexities than those in (a). In addition to the head wave marked by the first black line, there is coherent energy between the head and direct *P* arrival, outlined by black lines at distances greater than 9.5 km. From McGuire & Ben-Zion (2005).

network. As demonstrated in the subsequent sections, the assumed model of two juxtaposed vertically layered quarter-spaces can be used to invert the observed *P* and head arrival times at the scale of the observations to a stable sharp image of the velocity contrast across the fault at depth. To explore how additional complexities affect the results, we perform a suite of inversions using various data subsets, along with some synthetic waveform fits in a related model that includes FZ layers.

2 METHOD

2.1 Traveltimes

The FZ head and direct *P*-wave arrival times were picked by hand with each waveform being examined at least twice to increase consistency. For events on the slow side of the fault within the critical distance (eq. 1), the waveforms are characterized by an emergent first arriving head wave, opposite in polarity to that expected for a right-lateral strike-slip event located on the SAF, followed by a larger amplitude direct *P* wave with the expected polarity. Fig. 5(a) shows a set of velocity seismograms from events at various distances to the north of station SUM, located 1–2 km from the fault on the slow side (NE) of the fault. The waveforms are aligned on their *P*-wave arrival time and display an increase in the time between the head and direct *P*-wave arrival with propagation distance along the fault. For an interface between two different quarter spaces, this differential arrival time (Δt) grows with the distance travelled along the fault (r) as

$$\Delta t \sim r\left(\frac{1}{\alpha_2}-\frac{1}{\alpha_1}\right) \sim r\left(\frac{\Delta\alpha}{\alpha^2}\right), \tag{2}$$

with α and $\Delta\alpha$ denoting the average and differential *P*-waves velocities, respectively (Ben-Zion & Malin 1991). Thus, if an average *P*-wave velocity can be accurately estimated, it can be used along with the gradient of the differential arrival time versus propagation distance curve to obtain a first order approximation for the strength of the velocity contrast ($\Delta\alpha$).

Fig. 6 shows the differences between the direct *P* and head wave arrival versus hypocentre distances for 32 of the stations on the slow side of the fault. The moveout gradients were estimated with

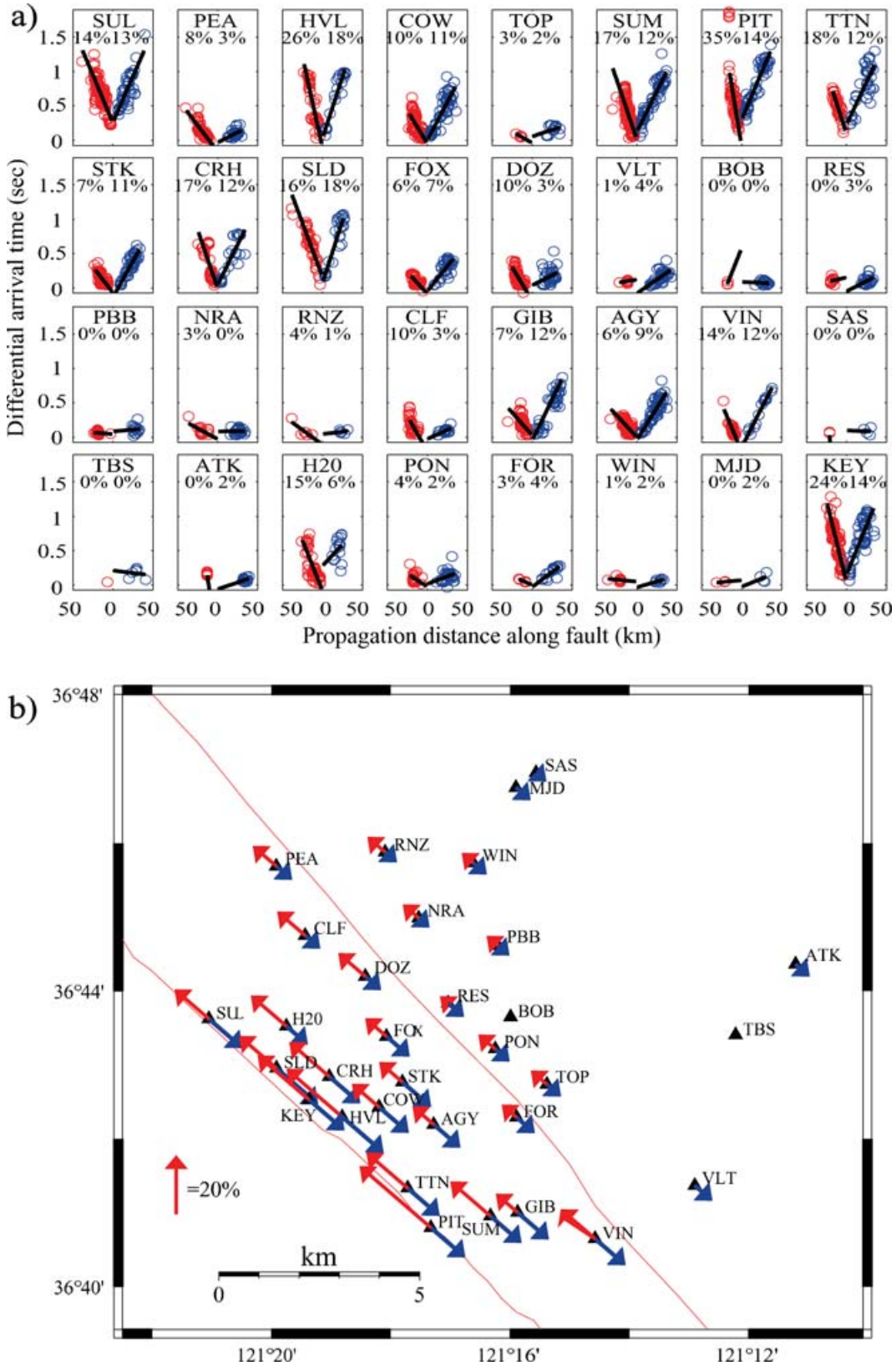

Figure 6. (a) Differential arrival times between the direct and head *P* waves as a function of along-fault propagation distance for 32 stations on the slow side of the fault. The red circles give results from events located to the northwest and blue circles from events to the southeast of the station. The black lines are least-squares fits to the points, giving (for those with enough data) estimates of the average velocity contrasts to the NW and SE. The obtained average velocity contrasts in percent are marked at the top of each panel. (b) A map view with the stations as triangles and the major faults as red lines. The velocity contrasts estimated in (a) at each station position, plotted as an arrow whose length corresponds to the size of the contrast estimated from events in the indicated direction (using same colours as in (a)).

a least-squares fit. The maximum differences of differential arrival times for events at the same station and similar distances range from −0.5 to +0.5 s. Stations closest to the fault, such as KEY and PIT have the highest residual to the least-squares fits. It is typically quite difficult to accurately pick arrival times at these stations because the signal-to-noise ratio is lower and the waveforms are more emergent and/or complicated. This can perhaps be attributed to the damage zone around the fault and near-nodal position of the stations in the *P*-wave radiation pattern. For some stations, usually those further from the fault, there are insufficient head wave first arrival picks to constrain the moveout velocity. Taking these available gradient estimates and an average velocity of 5 km s^{-1} (McGuire & Ben-Zion 2005), the average velocity contrast for each station can be estimated using eq. (2). The velocity contrast estimates (labelled in Fig. 6a) show that stations generally measure a higher contrast from events to the north of a given station (shown in red), and that stations closer to the fault are affected by higher contrast values than those further away (Fig. 6b). The largest average contrast is about 35 per cent at station PIT which is within 200 m of the fault. The largest value might reflect the contrast between the low velocity damage zone associated with the fault, on which this station likely resides, and the faster side of the fault. More typical values are in the 10–20 per cent range, which perhaps better represents the true contrast in velocity between the host rocks on the opposite sides of the fault.

2.2 Joint inversion of FZHW and direct *P* arrivals

To obtain more accurate estimates of the velocity contrast across the SAF, accounting for depth-variations, we perform a joint inversion of the FZHW and *P*-wave arrival time data. The model consists of two vertically layered quarter-spaces that represent the two crustal blocks on the opposite sides of the fault (Fig. 1). For simplicity, the number of layers in each block is kept constant leaving the thicknesses and velocities of the layers as free model parameters. We employ the ray tracing procedure and the adjusting random search inversion algorithm of Ben-Zion *et al.* (1992). The adjusting random search is similar to simulated annealing, but uses a fixed (rather than progressively decreasing) maximum perturbation of parameters. In an earlier phase of the work we found that the adjusting random search method, with a maximum perturbation size tailored to properties of the data by trial and error, produces a smaller misfit than inversions with the same number of iterations using progressively decreasing maximum perturbation similar to simulated annealing. Additional details on the inversion algorithm can be found in Ben-Zion *et al.* (1992).

The traveltimes for the direct and head waves to the various stations are calculated for the model shown in Fig. 1 with the following expressions (Ben-Zion *et al.* 1992). For the direct *P* wave, the traveltime t_d is

$$t_d = \xi \cdot p + \sum \zeta_j \sqrt{\alpha_j^{-2} - p^2}, \tag{3}$$

where ξ is the horizontal component of the straight source–receiver line, p is the component of slowness along ξ, and ζ_j and α_j are the vertical component of the ray path and the *P*-wave velocity in medium j, respectively. For the head wave, the traveltime t_h is

$$t_h = \left[y \cdot p + \sum \zeta_{fj} \sqrt{\alpha_{fj}^{-2} - p^2} \right] + x \sqrt{\alpha_{s1}^{-2} - \alpha_{f1}^{-2}}, \tag{4}$$

where y is the component of the source–receiver separation along the fault, p is the y component of slowness, ζ_{fj} and α_{fj} are, respectively, the vertical component of the ray and *P*-wave velocity in medium j on the faster side of the fault, and α_{f1}, α_{s1} denote the *P*-wave velocities of the top layers on the faster and slower sides of the fault, respectively. The calculated traveltimes are used to backcalculate model origin times of the recoded earthquakes via subtraction from the measured arrival times. The difference between the modelled origin times of each earthquake, calculated with each of the available direct and head wave arrival times, gives a measure of how well the model approximates the true structure. The model origin times based on all the available data form a model error function *Merr* given by:

$$Merr(F) = \sum_{i=1}^{eq} \sum_{j=2}^{d(i)+h(i)} \sum_{k=1}^{j-1} abs\,[O(i,j) - O(i,k)], \tag{5}$$

where F is a vector containing the model parameters and *eq* is the total number of earthquakes. The indexes $d(i)$ and $h(i)$ denote, respectively, the number of direct and head wave time picks made for earthquake i, $O(i, j)$ is the origin time of earthquake i calculated using the station j observed direct wave $[j \leq d(i)]$ or head waves $[j > d(i)]$ arrival times and corresponding model calculated traveltimes. Since this model error would increase with an increasing number of data points, it is normalized by the number of origin times used in its calculation to create *NMerr,* the mean mismatch per a single used pair of arrival time data for the same event. The search of best fits to both head and direct wave arrivals involves minimization of the normalized error *NMerr*, using a self-adjusting random search where the layer thicknesses and velocities are perturbed at every inversion iteration (see additional details in Ben-Zion *et al.* 1992).

To maximize the efficiency of the inversion and to tailor the values of maximum perturbation size to properties of parameters in the inversion, we perform tests using a data set of synthetic arrival times, calculated using the real event and station locations. The inversion parameters that can be tuned to lead most efficiently to the minimum model misfit are the number of iterations, the size of the maximum random perturbations to the model parameters (layer velocities and thicknesses), and the initial values of the parameters. While the latter should have little impact in the limit of a large number of iterations, the effects of the other choices should be explored.

Fig. 7 shows how the size of the maximum employed random perturbation changes the size of the final normalized error for different numbers of iterations. The calculations are done using the two different layered quarter-spaces obtained by Ben-Zion *et al.* (1992) for the Parkfield section of the SAF. When the absolute value of the maximum perturbation is above 0.2, the final error is increasing. The lowest final error is for a maximum perturbation between 0.1 and 0.15. Increasing the number of iterations from 1000 to 2000 improves the fit and reduces the error. There is some improvement between 2000 and 3000 iterations, but no further reduction is found in the region with the best maximum perturbation beyond 3000 iterations. Assuming that the synthetic calculations are representative of the features of the data, values of 3000 iterations and maximum perturbation of 0.1 appear to offer the best chance of rapidly finding the global minimum. The assumed velocity model used in the synthetic calculation, and the best-fitting model obtained by an inversion using the above parameters and starting with the standard five-layers 1-D velocity model used to locate events in that area, are shown in Fig. 8. Further synthetic tests and explanation of the improvement in resolution from the incorporation of head waves can be found in Ben-Zion *et al.* (1992).

As discussed earlier, the relocated seismicity in the study area falls onto a narrow near-vertical zone to the southwest of the surface trace of the SAF. However, these locations are not consistent with the first

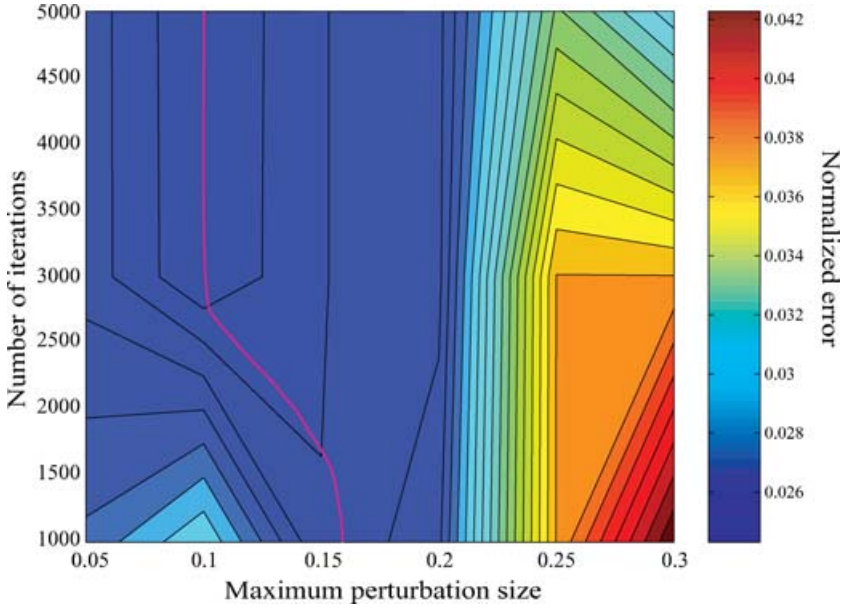

Figure 7. A contour plot summarizing the ability of the inversion to minimize the error in synthetic data sets. The absolute value of the maximum perturbation size (*x*-axis) and number of iterations (*y*-axis) are adjustable parameters of the inversion. The local minimum of the normalized error for different sets of values is plotted as a red line.

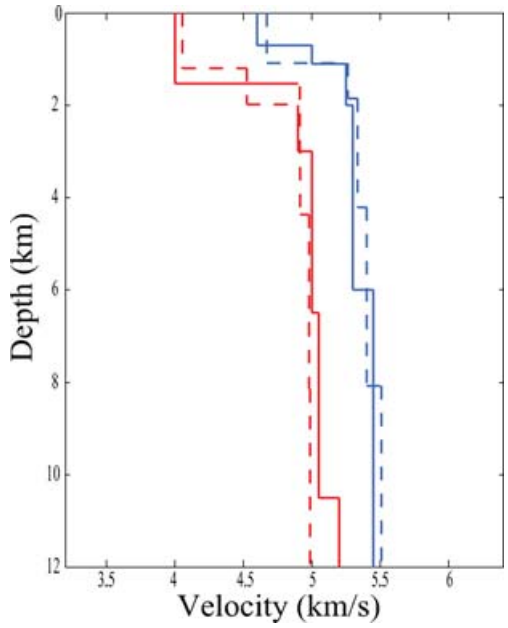

Figure 8. Inversion of synthetic data generated using the event and station locations of the temporary deployment and the velocity structure obtained by Ben-Zion *et al.* (1992) for the Parkfield section of the SAF. The dashed lines give the velocity profiles used in the generation of the synthetic arrival times for the fast (blue) and slow (red) sides of the fault. The solid lines are the recovered velocity structure using the inversion method outlined in the text.

motion polarities at instruments within 100 m of the fault. The first motion polarities are fit properly by assuming that the events are on a vertical plane under the surface trace of the fault. As mentioned in the introduction, to resolve the discrepancy between the catalogue locations and first motion polarities, we moved the vertical plane defined by the seismicity 700 m northeast such that it intersects with the known surface trace location relative to station PIT. To test the possible effects of this shift on our results, a series of inversions were carried out on the observed data assuming event locations at various distances from the surface trace. The set up for the inversions is the same as that described in Section 3 as set (B3), and it consists of 24 stations located at over 2 km from the surface trace, selected to have approximately equal numbers of phase arrivals on the slow and fast sides of the fault. The event locations are shifted within a zone that is 1000 m wide and 10 inversion runs are performed for each assumed configuration. Fig. 9 shows how the depth-average velocity contrast for each set of inversions changes as a function of the distance of the assumed event locations from the surface trace of the SAF. Within the range over which the events are shifted, the average velocity contrasts changes by only 1 per cent out of average contrasts of about 26 per cent. Hence the 700 m shift required for consistency of motion polarities has very small effect on the inversion results.

3 RESULTS

We perform inversions using data generated by 450 events picked at up to 53 stations, resulting in over 9800 direct and 2700 head *P*-wave arrival time picks. These are utilized in six sets of inversions that are performed on the whole data set (A), using stations which are within 5 km (B1), within 2 km (B2) and further than 2 km (B3) from the fault, and finally using events to the northeast of the complexity (C1) or events within and to the southeast of the complexity (C2). Initially, a five layer model was used but the inversions always reduced the thickness of one of the layers to near 0. Thus all results presented are for four layers. The starting model in all cases (dashed black line in Fig. 10a) was the Northern California velocity structure given out with the hypoDD program by the USGS.

Fig. 10(a) shows the results from 10 inversion runs using all the data (set A), with each inversion run performed using a different sequence of random numbers for the self-adjusting random search. The solid coloured lines represent the model with the lowest misfit, while the dashed coloured lines and grey shaded areas represent the mean and standard deviation associated with the 10 inversion runs.

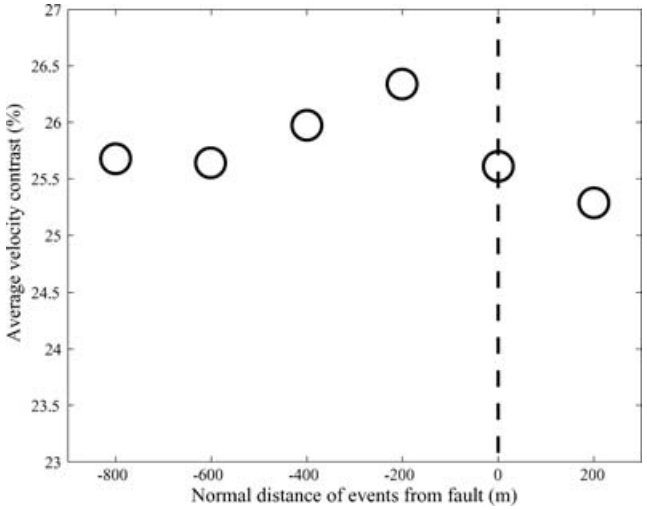

Figure 9. Depth-average velocity contrasts (circles) obtained by sets of inversions assuming the fault at depth is located at different normal distances from the surface trace of the San Andreas Fault. Negative and positive horizontal coordinates are distances perpendicular to the surface trace (black dashed line) in the southwest and northeast directions, respectively. The events are assumed in this study to be below the surface trace, some 700 m from their catalogue locations.

A general feature of the models is a subsurface layer (depth <1 km) on the fast side of the fault. Although this layer is very thin, it is a common feature of the inversion results (Fig. 10b). However, the ranges of depths and velocities covered by the uncertainties in the top two layers of Fig. 10 imply that the thin subsurface layer is not well constrained by the inversions. Between 1 and 3 km the velocity contrast between the two sides of the fault increases to its highest values, with the velocity of the slow side only 50 per cent of the fast side. At greater depths the velocity difference across the fault remains fairly constant at approximately 1 km s^{-1} or between 10 and 20 per cent. The average values of the depths and velocities are consistent overall with the previous tomographic study of Thurber *et al.* (1997), as well as with synthetic waveform fits obtained by forward modelling in the end of the section.

To constrain further the velocity structure in the immediate vicinity of the fault, additional inversions are performed (Fig. 11) using subsets of instruments located closer and closer to the fault (sets B1–B3). More prominent shallow low velocity layers emerge for both sides of the fault, and become significant features outside the range of the uncertainties when inversions are performed using only near fault instruments (Fig. 11d). In the inversion using all the stations, those further from the fault are not affected by a low velocity FZ layer above the seismicity of the type imaged by recent studies with FZ trapped waves (Ben-Zion *et al.* 2003; Peng *et al.* 2003; Lewis *et al.* 2005). In contrast, near-fault stations would be affected by such a FZ layer and will produce a modification in the inversion results.

When subsets of stations within 5 and 2 km of the fault (Figs 11c and d) are used, a larger proportion of the ray paths are affected by the internal FZ structure, and the results more strongly reflect the structure in the immediate vicinity of the fault. The results from those inversions imply a shallow low velocity layer on the faster side of the fault. This feature becomes increasingly more evident as the number of stations closer to the fault increases (Figs 11a–d), and it appears to be well-constrained outside the variations of model results obtained by different inversion runs. For the slower side of

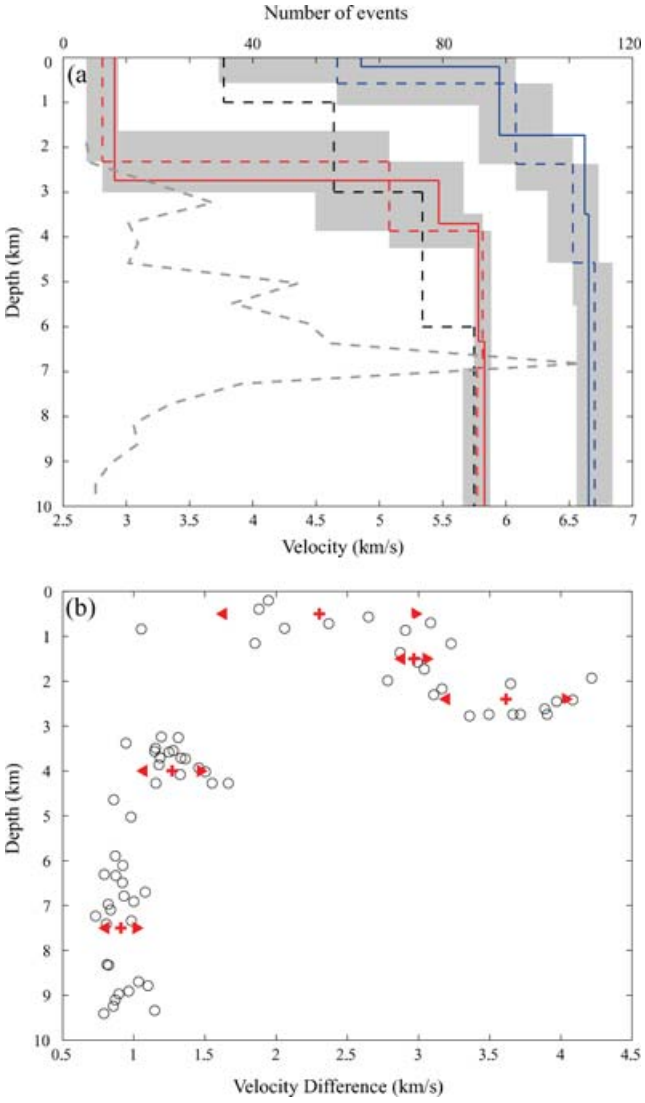

Figure 10. (a) Inversion results of *P*-wave velocities versus depth on the SAF using all the stations and data. (a) The solid red and blue lines are the best-fitting velocity profiles for the slow and fast sides of the fault, respectively, out of 10 inversion runs performed on the data. The dashed red and blue lines are the average depth and velocity of each layer from all 10 inversions, and the grey shaded area around the mean represent the standard deviation of the depth and velocity of that layer. The dashed black line is the initial velocity model used in the inversions. The dashed grey line and horizontal axis on top give the number of events as a function of depth. (b) The differences between the velocities on the fast and slow sides of the fault, plotted at the depth where that contrast occur for each of the 10 inversion runs. The mean and standard deviation of the values at that depth are plotted with the red symbols.

the fault, the results show a corresponding shallow low velocity zone only with inversions using just the stations within 2 km of the fault (Figs 11d and e). The results may be affected in part by the different takeoff angles and ray paths from the earthquakes to the different stations. However, synthetic model calculations with two layered quarter-spaces and the used earthquake and station locations indicate that the trends seen in Fig. 11 are unlikely to be produced as an artifact of the employed subsets of stations.

The final two sets of inversions involve events to the northwest (C1) and to the southeast (C2) of the array. While the results based

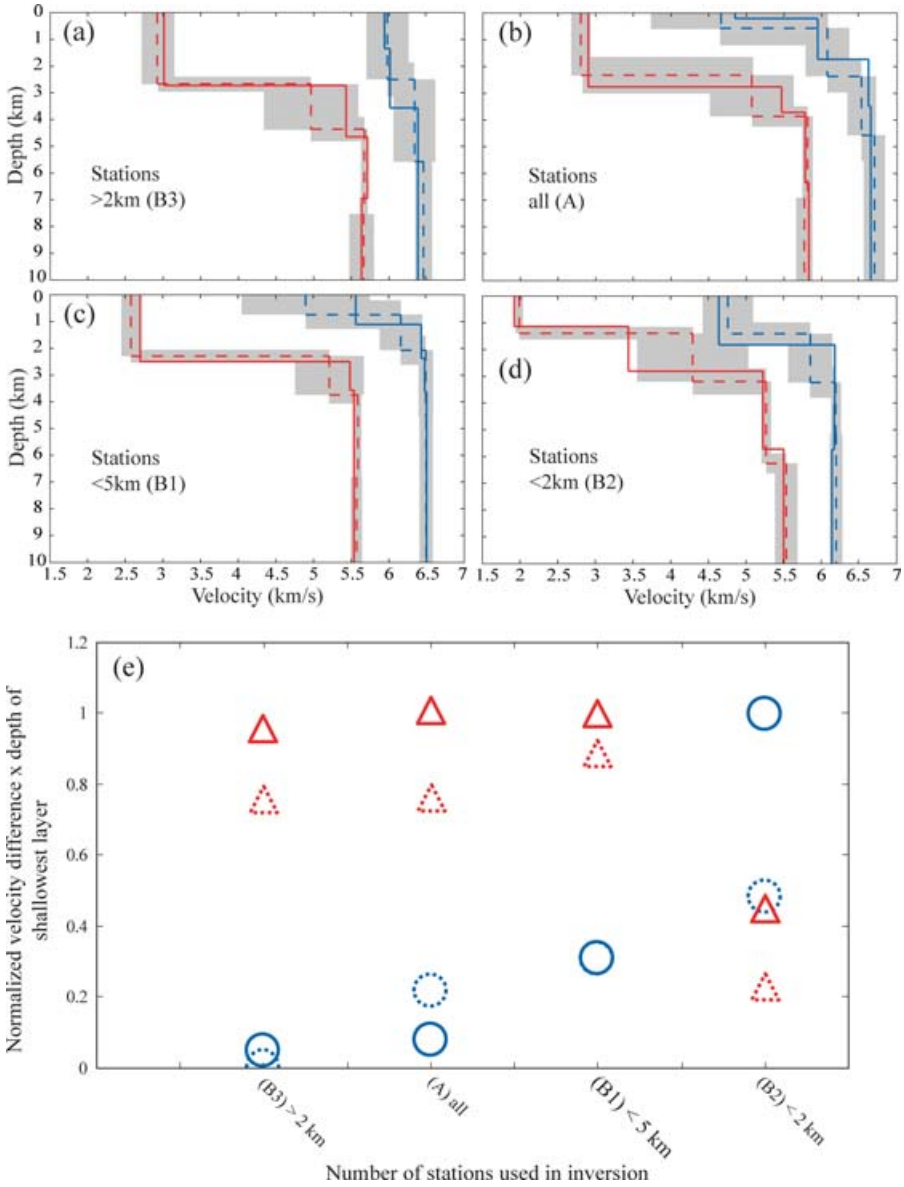

Figure 11. (a) Results from inversions on four different sets of data associated with increasing numbers of near-fault stations. (a) Stations further than 2 km from the fault, (b) all stations, (c) only stations within 5 km and (d) only stations within 2 km. The solid and dashed lines represent the minimum misfit and mean values from 10 sets of inversions, while the grey area gives the standard deviation of depth and velocity. (e) The value of the velocity difference between the top layer and the one below it, normalized to the maximum velocity difference, and multiplied by the depth of the top layer. This quantity represents the characteristics of the top most layer of the velocity structure and it changes in a systematic manner in the inversion sets (a–d). The triangles (red) and circles (blue) are for the slow and fast sides, respectively. The dashed and solid symbols represent the best-fitting and mean model results, respectively.

on events to the northwest (Fig. 12) are very similar to the inversion results of all events (Fig. 10), the results based on the subset to the southeast (Fig. 13) have some distinct features. The velocity of the faster side of the fault below 4–5 km is between 0.5 and 1 km s^{-1} faster, while the shallowest layer extends to a greater depth (1–1.5 km) than in the other inversions. In the depth range 6–8 km, the velocities on both the fast and slow sides of the fault show a reduction with depth that is significant enough to be visible within the variations of the different inversion runs. These features probably reflect properties of the sliver of high velocity granite in the southeast area discussed by McGuire & Ben-Zion (2005). The variations of results from the inversion runs using the data set C2 are larger (Fig. 13b) than in the other cases, showing as expected that the data from the southeast are harder to fit with our model.

The inversions of the arrival time data discussed so far give the depth variations of laterally-averaged velocity contrasts between regions on the opposite sides of the fault containing the employed events and stations. We now discuss waveform modelling of the seismic phases in the early portions of the observed waveforms (Fig. 14), using a complementary model representing the depth-averaged lateral velocity variations in the immediate vicinity of the fault. The synthetic calculations are performed with the 2-D analytical solution of Ben-Zion & Aki (1990) and Ben-Zion (1998) for the scalar wave equation in a model having one or two vertical layers between two quarter spaces. The source consists of an *SH* line dislocation with a unit step in time and the solution assumes particle motion parallel to the structural interfaces, allowing fault parallel and vertical synthetic to be generated. This results in the solution

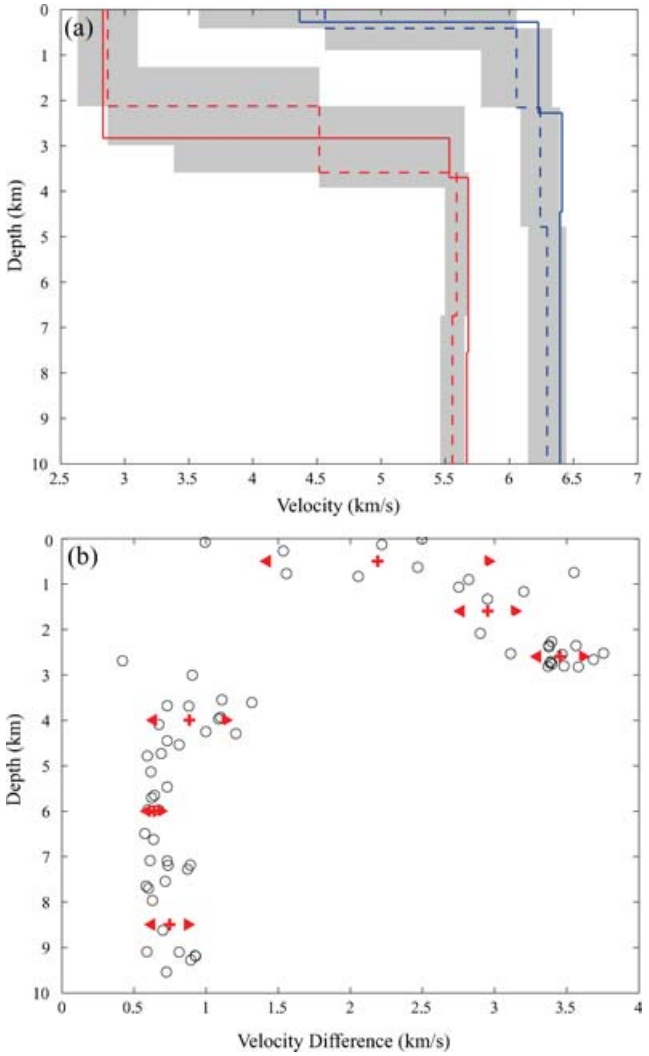

Figure 12. (a) The four-layer velocity models for the opposite sides of the fault produced by inversion for a subset of events in the central and northwestern part of the study area. The solid lines are the results with the lowest misfit, the dashed lines are the average of the results from 10 inversion runs using the same set-up, and the grey area is the standard deviation. (b) The velocity difference between the layers in all of the inversion runs used to obtain the average result in (a) as a function of depth. The mean and standard deviation of the values at a given depth are plotted with the red symbols.

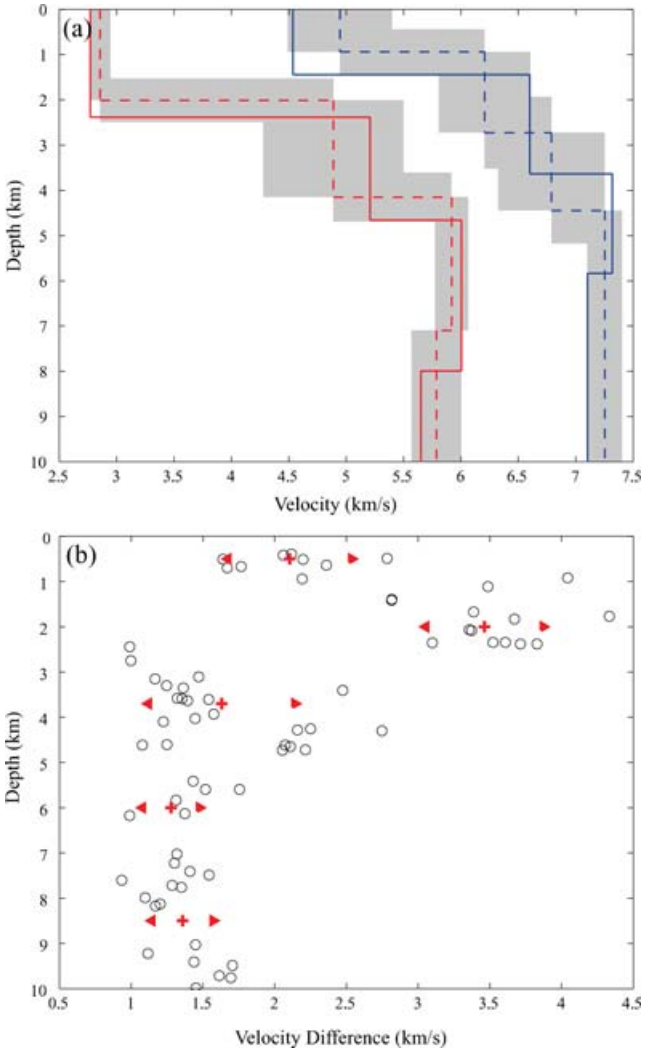

Figure 13. (a) The four-layer velocity models for the opposite sides of the fault produced by inversion for a subset of events in the southeastern part of the study area. (b) The velocity difference between the layers in all of the inversion runs used to obtain the average result in (a). The notations are the same as in Fig. 12.

being suitable only up to the direct *P* wave arrival, after which *P-SV* conversions and additional phases become important parts of the seismograms.

The stations used in Fig. 14 were chosen to have similar source–receiver distances along the fault but different normal distances from the fault. The arrival times and amplitudes of the direct *P* waves at the stations are controlled by the average velocity and *Q* values of the crustal blocks on which they reside, while the properties of the head waves at stations on the slow side depends on the attributes of both crustal blocks. The relative times, amplitudes and motion polarities of the various phases depend also on the propagation distance along the fault and the receiver offset from the fault. These parameters are determined from the assumed values of the source and receiver locations that were used in the previous arrival time analysis. To increase the spatial resolution of the results, the fit to each seismogram in Fig. 14 is produced individually with different structural parameters. In most cases, the synthetic waveform fits to the early portions of the *P* waveforms require only two quarter spaces. As discussed by McGuire & Ben-Zion (2005), for arrivals at stations near the fault and events located in the region with the fault complexity, an intermediate velocity layer is needed to account for the energy between the head and direct *P* waves. Incorporation of such a layer in the model produces an additional FZ phase that is seen clearly in both the observed and synthetic waveforms at station PIT in Fig. 14. In the next section, we discuss the results obtained by the arrival time inversions and waveform modelling in the context of a physical model of a fault separating two different crustal blocks and other available velocity images for the region.

4 DISCUSSION

Fig. 15 provides a schematic representation of the general features of the near-fault velocity structure in the Cienega Valley to Bear Valley region of the SAF, based on the arrival time inversions and waveform modelling done in this work. The abundant observations of head

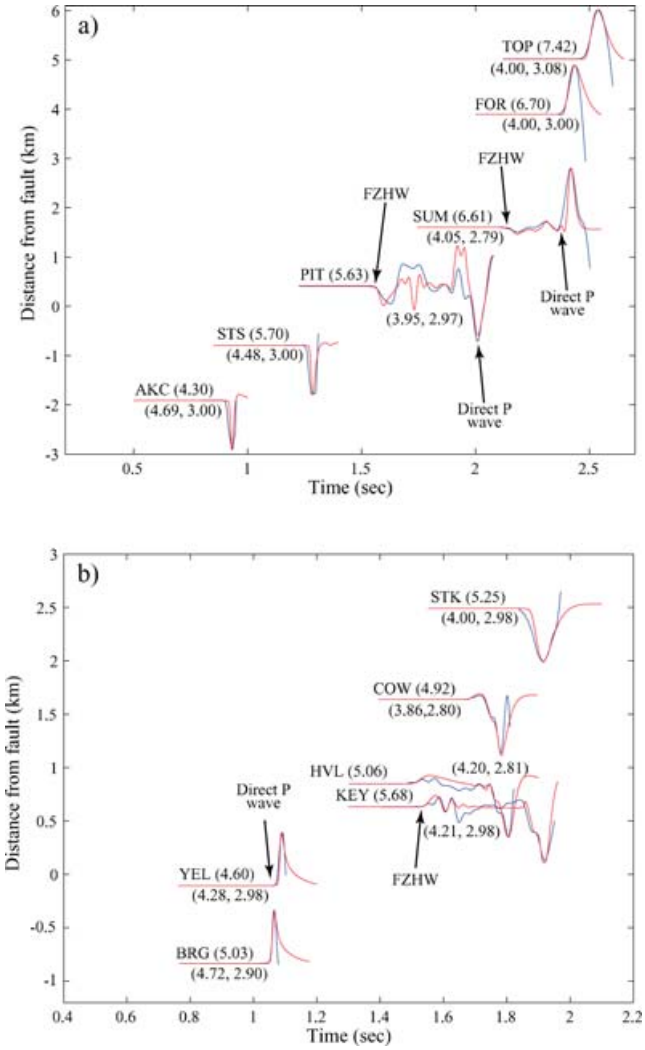

Figure 14. Observed (blue) and synthetic (red) velocity seismograms for stations on the fast and slow sides of the fault. The synthetic waveforms are calculated using the 2-D analytical solution of Ben-Zion (1998) for line dislocation with a unit step function in time at the interface between two different quarter-spaces with possible vertical layers in between. Each pair of seismograms is labelled with the station name followed by the hypocentral distance in parenthesis. Some of the direct *P* and FZHW arrivals are indicated by arrows with corresponding labels. The *P*-wave velocities in km s^{-1} of the quarter-space used to generate the synthetic seismograms are given in parenthesis under the waveforms. The employed *Q* values are 60 and 30 for the fast and slow sides of the fault, respectively. (a) Seismograms associated with an event in the complex area to the SW of the array. (b) Seismograms associated with an event in the simpler central area.

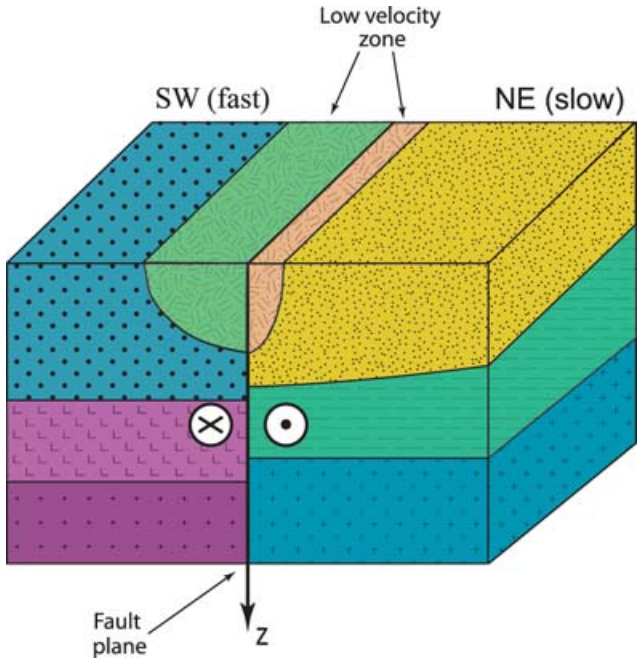

Figure 15. A schematic diagram of the inferred velocity structure in the study area, consisting of two layered quarter-spaces, joined along a sharp material interface, and a shallow asymmetric low velocity zone around the fault. The colours represent the media velocities, with violet being the fastest and orange being the slowest.

waves imply that a sharp near-planar interface between materials with differing properties exists on this portion of the fault. We further observe a high velocity contrast in the shallow structure, a large increase in velocity around 3 km on the slower side of the fault, and a decreasing velocity contrast with depth. All the sets of inversion consistently show high velocity contrasts (∼50 per cent) above 3 km, while below this depth the variation across the fault reduces to about 10–20 per cent. Between these two depth ranges, the velocity on the slower side increases in a single large step of 2–2.5 km s^{-1}. Sets of inversions with 5, 6 and 8 layers were attempted to estimate how sharp or gradual this transition is. However, the inversion results always produce profiles of the type shown in Fig. 10. This feature of the results remains largely unchanged within the inversion sets (B1)–(B3), implying that it is not a structure associated with the immediate vicinity of the SAF such as a low velocity trapping structure.

The arrival time inversion of Thurber *et al.* (1997) shows a region of 3–4 km s^{-1} *P*-wave velocity extending 6 km to the NE of the fault and down to 3–4 km depth. This region may represent the same structural feature seen in our inversions as a large velocity step at 3 km depth on the slow side. The sharp velocity increases in our inversions probably reflect geological transitions, perhaps exaggerated somewhat by the assumed layered structure and limited inversion resolution. Additional data generated by events around 3 km depth could lead to a more gradual velocity changes with depth. Other possible structural elements that could explain the top section include a region of high fluid content, and thus presumably cracks and damage, that was imaged during a magnetotelluric study down to a depth of 2–4 km in the 6 km interval between the SAF and the Calaveras fault to the northeast (Bedrosain *et al.* 2004).

The inversions also show finer results, such as structural complexities in the FZ and the possible existence of an asymmetry of rock damage across the fault. To the southeast of the array the fault splits into two distinct branches, with shallow seismicity on the east branch and at approximately 6 km depth a switch to seismicity located on the more westerly branch (Fig. 4). Based on waveform and traveltime analysis, combined with geological surface mapping, McGuire & Ben-Zion (2005) conclude that this represents a sliver of granite between the two fault branches separating the granites and volcanic rock of the southwest (fast side) from the sedimentary rocks on the northeast (slow) side of the fault. The inversion results based on the 150 events to the southeast (set C2) that are within or have paths through this complexity show at 6–8 km depth a reduction in velocity (Fig. 13). This corresponds to the depth at which the seismicity changes from one fault branch to the other. The character of waveforms that pass through this area is also different

(Fig. 5), with additional phases occurring between the FZHW and direct *P* arrivals. The synthetic waveform modelling of Fig. 14 (see also McGuire & Ben-Zion 2005) demonstrates that the additional phases can be explained by a vertical layer with intermediate velocity between those of the bounding quarter-spaces, which represents the sliver of granite.

While it is interesting that our simple model can distinguish features on the scale of approximately 200 m, and further confirm the existence of the complexity in the structure, it can provide little more quantitative results on the nature of the complexity without becoming more complex itself. The mapping of event locations in the model onto a single interface affects the accuracy of the results, primarily for the structure on the fast side of the fault. The propagation distances from the events on the deeper fault branch to the stations on the fast side are in reality smaller than those used in the model with data set C2 (Fig. 13). This produces somewhat unrealistically high velocities for the deepest layer of ∼7.2–7.4 km s^{-1} compared to the ∼6.6–6.8 km s^{-1} for the same depth range obtained by Thurber *et al.* (1997). This would also impact the inversion results using the set A containing all the data, so the velocities of the deepest layers are probably slightly increased. The velocity below 4 km of 6.2–6.4 km s^{-1} in Fig. 12 from inversions using the data set C1 that does not contain the branched section of the fault might provide the closest representation of the true structure.

When using subsets of the data with increasing proportions of stations close to the fault (sets B1–B3), the inversions show increasingly clearer near-surface low velocity (damage) structures, with the low velocity surface layer on the faster side more readily evident at a greater range of distances. This is seen by examining the results obtained by four sets of inversions (Figs 11a–d), and is also reflected by plotting (Fig. 11e) the obtained depth and velocity of the shallowest layer on each side of the fault. As shown in Fig. 11(e), these two defining parameters of the surface layers remain largely unchanged on the slower side of the fault (triangles) until only stations within 2 km are used, whereas on the faster side (circles) the low velocity surface layer grows systematically. There is no apparent consistent variation in the properties of any of the deeper layers with changes in proximity to the fault. The larger the fraction of near fault stations that are used in the inversions, the more the images of the shallow layers reflect the velocity structure of the near fault region, particularly as there is an increase in the relative number of head wave arrivals. Since the results characterizing the shallowest model layers are correlated clearly with the proximity of the employed receivers from the fault, it is reasonable to assume that the imaged low velocity material represents a damage FZ layer like that seen in trapped wave studies.

The average velocity profile for the upper 3 km should be the most well constrained as all the rays from all the events pass through it. However, since this zone resides above the shallowest seismicity (2–3 km), the internal variations within the shallow low velocity layers cannot be resolved, except to say that they do not extend below 3 km depth. We note that we obtain good fits for the arrival time, polarities and amplitude of the head and direct waves (Fig. 14) using quarter-space velocities of ∼3 km s^{-1} on the slow side and ∼4.5 km s^{-1} on the fast side. These values are broadly consistent with the near fault velocities at shallow depth obtained in the arrival time inversions and also those from Thurber *et al.* (1997). In the tomographic images of Thurber *et al.* (1997), the FZ may be associated with a vertical structure in the *P*/*S*-wave velocity ratio. It is interesting to note that this vertical structure in the results of Thurber *et al.* (1997) is also offset to the SW from the surface trace of the fault, in agreement with the asymmetry of the shallow structure in the results of Fig. 11.

The same asymmetry is also evident in the parameters used to obtain the synthetic waveform fits of Fig. 14 for the two shallow events with depths of ∼3 km at a number of near fault stations. The shallow events are in the depth range where the structure may be well represented by two quarter spaces separated by a low velocity layer. As indicated in Fig. 14, the velocities required to fit the direct *P* arrival times generally reduce with proximity to the fault. The gradient of the velocity reduction with increasing proximity to the fault is particularly strong on the faster side. Lower velocities on the fast side of the fault are also required to obtain the correct head wave arrival times, implying that the *P*-wave velocities at the material interface are lower again than at stations within a few hundreds of metres SW of the fault. These observations imply, like the changes in the results of Fig. 11, that the shallow low velocity layer is not centred on the SAF, but is rather asymmetrically located mostly on the faster side of the fault.

A shallow asymmetric damage zone, with more damage on the faster side of the fault, is an expected outcome of ruptures on an interface that separates different elastic media (Ben-Zion & Shi 2005). Such ruptures tend to propagate preferentially and/or more vigorously in the direction of slip on the slower side of the fault (e.g. Weertman 1980; Ben-Zion 2001; Shi & Ben-Zion 2006; Rubin & Ampuero 2007), and they produce damage-generating tensile radiation consistently on the faster side. Significant damage generation is limited to the top few kilometres of the crust (Ben-Zion & Shi 2005), since increasing normal stress suppresses the damage generation. Our inference that the observed asymmetric shallow structure is associated with a preferred propagation direction of earthquakes on the SAF south of Hollister is compatible with observations of Rubin & Gillard (2000) of asymmetric along-strike distribution of aftershocks in this section of the fault. We also note that similar asymmetric damage zones, which are offset to the faster side of the fault, were recently observed in inversions of trapped waves on the San Jacinto fault (Lewis *et al.* 2005) and detailed geological mapping in the structure of several faults of the southern San Andreas system (Dor *et al.* 2006a; Dor *et al.* 2006b). The asymmetry of the shallow fault zone structures may be associated with other features and mechanisms, such as local topography and various site effects. However, at present the most consistent explanation for the available diverse observations appears to be a preferred propagation direction of earthquake ruptures.

As noted by Ben-Zion *et al.* (1992) and in Section 3, analyses of FZ head and trapped waves complement each other in high-resolution imaging of FZ structures. The head waves can provide depth profiles of the overall velocity contrast across the fault, while the trapped waves can be used to obtain the depth-averaged lateral variations of the structure. The sensitivity of near-fault head waves to the internal FZ structure can help to reduce some of the non-uniqueness in trapped-wave inversions. Additional important information on the material and geometrical properties of fault zones can be obtained using other potential signatures of damaged rocks such as anisotropy and scattering (e.g. Boness & Zoback 2004; Liu *et al.* 2004, 2005; Cochran *et al.* 2006; Peng & Ben-Zion 2005, 2006) . A combined use of phases generated by material interfaces and damaged FZ rocks, direct body waves, and accurate absolute event locations, has the potential to provide unparalleled detailed images of FZ structures and their surrounding environment. Our results indicate that the inclusion of FZ head waves in inversions of seismic data for the structure of large FZs can increase considerably the resolution of the velocity contrast across the fault as a function

of depth. We also note that proper accounting for fault zone head waves can improve the accuracy of focal mechanisms determined from data collected by near-fault arrays (e.g. Ben-Zion & Aki 1990; Kilb & Hardebeck 2006).

ACKNOWLEDGMENTS

We thank the IRIS Data Management Center and the Northern California Earthquake Data Center for distributing the employed dataset. The manuscript benefited from useful comments by the editor J. Trampert and three anonymous referees.

REFERENCES

Aki, K. & Lee, W.H.K., 1976. Determination of three-dimensional velocity anomalies under a seismic array using first *P* arrival times from local earthquakes, Part 1: a homogeneous initial model, *J. Geophys. Res.*, **81**, 4381–4399.

Andrews, D. & Ben-Zion, Y., 1997. Wrinkle-like slip pulse on a fault between different materials, *J. Geophys. Res.*, **102**, 55–571.

Bakun, W.H., Stewart, R.M., Bufe, C.G. & Marks, S.M., 1980. Implications of seismicty for failure of a section of the San Andreas fault, *Bull. Seim, Soc. Am.*, **70**, 185–201.

Bedrosain, P.A., Unsworth, M.J., Egbert, G.D. & Thurber, C.H., 2004. Geophysical images of the creeping segment of the San Andreas Fault: implications for the role of crustal fluids in the earthquake process, *Tectonophysics*, **385**, 137–158.

Ben-Zion, Y., 1989. The response of two joined quarter spaces to SH line sources located at the material discontinuity interface, *Geophys. J. Int.*, **98**, 213–222.

Ben-Zion, Y., 1990. The response of two half spaces to point dislocations at the material interface, *Geophys. J. Int.*, **101**, 507–528.

Ben-Zion, Y., 1998. Properties of seismic fault zone waves and their utility for imaging low velocity structure, *J. Geophys. Res.*, **103**, 12 567–12 585.

Ben-Zion, Y., 2001. Dynamic ruptures in recent models of earthquake faults, *J. Mech. Phys. Solids*, **49**, 2209–2244.

Ben-Zion, Y. & Aki, K., 1990. Seismic radiation from an SH line source in a laterally heterogeneous planer fault zone, *Bull. Seism. Soc. Am.*, **80**, 971–994.

Ben-Zion, Y. & Malin, P., 1991. San Andreas Fault zone head waves near Parkfield California, *Science*, **251**, 1592–1594.

Ben-Zion, Y. & Andrews, D.J., 1998. Properties and implications of dynamic rupture along a material interface, *Bull. Seism. Soc. Am.*, **88**, 1085–1094.

Ben-Zion, Y. & Shi, Z., 2005. Dynamic rupture on a material interface with spontaneous generation of plastic strain in the bulk, *Earth Planet. Sci. Lett.*, **236**, 486–496, doi:10.1016/j.epsl.2005.03.025.

Ben-Zion, Y., Katz, S. & Leary, P., 1992. Joint inversion of fault zone head and direct *P* arrivals for crustal structure near major faults, *J. Geophys. Res.*, **97**, 1943–1951.

Ben-Zion, Y. et al., 2003. A shallow fault zone structure illuminated by trapped waves in the Karadere-Duzce branch of the north Anatolian Fault, Western Turkey, *Geophys. J. Int.*, **152**, 699–717.

Boness, N.L. & Zoback, M.D., 2004. Stress-induced seismic velocity anisotropy and physical properties in the SAFOD Pilot Hole in Parkfield, CA, *Geophys. Res. Lett.*, **31**, L15S17, doi:10.1029/2004GL019020.

Elizabeth, S., Cochran, E.S., Li, Y.-G. & Vidale, J.E., 2006. Anisotropy in the Shallow Crust Observed around the San Andreas Fault Before and After the 2004 **M** 6.0 Parkfield Earthquake, *Bull. Seism. Soc. Am.*, **96**, S364–S375, doi:10.1785/0120050804.

Dibblee, T.W., 1974. Geologic map of the Salinas quadrangle, California, in Open-file report 74-1021, U.S. Geological Survey

Dor, O., Rockwell, T.K. & Ben-Zion, Y., 2006a. Geologic observations of damage asymmetry in the structure of the San Jacinto, San Andreas and Punchbowl faults in southern California: a possible indicator for preferred rupture propagation direction, *Pure Appl. Geophys.*, **163**, 301–349, doi:10.1007/s00024-005-0023-9.

Dor, O., Ben-Zion, Y., Rockwell, T.K. & Brune, J., 2006b. Pulverized Rocks in the Mojave section of the San Andreas Fault Zone, *Earth Planet. Sci. Lett.*, **245**, 642–654.

Eberhart-Phillips, D. & Michael, A.J., 1993. Three-Dimensional velocity structure, seismicity and fault structure in the Parkfield region, central California, *J. Geophys. Res.*, **98**, 15 737–15 758.

Ellsworth, W., 1975. Bear valley, California, earthquake sequence of February-March 1972, *Bull. Seism, Soc. Am.* **65**, 483–506.

Igel, H., Jahnke, G. & Ben-Zion, Y., 1997. Simulation of SH and P-SV wave propagation in fault zones, *Geophys. J. int.*, **128**, 533–546.

Jahnke, G., Igel, H. & Ben-Zion, Y., 2002. Three-dimensional calculations of fault zone guided waves in various irregular structures, *Geophys. J. Int.*, **151**, 416–426.

Kilb, D. & Hardebeck, J.L., 2006. Fault parameter constraints using relocated earthquakes: a validation of first motion focal mechanism data, *Bull. Seism. Soc. Am.* **96**, 1140–1158.

Korneev, V.A., Nadeau, R.M. & McEvilly, T.V., 2003. Seismological studies at Parkfield IX: fault zone imaging using guided wave Attenuation, *Bull. Seism. Soc. Am.*, **93**, 1415–1426.

Lewis, M.A, Peng, Z., Ben-Zion, Y. & Veron, F., 2005. Shallow seismic trapping structure in the San Jacinto Fault Zone, California, *Geophys. J. Int.*, **162**, 867–881, doi:10.1111/j.1365-246X.2005.02684.x.

Li, Y.G., Ellsworth, W.L., Thurber, C.H., Malin, P. & Aki, K., 1997a. Fault-zone guided waves from explosions in the San Andreas fault at Parkfield and Cienega Valley, California, *Bull. Seismol. Soc. Am.*, **87**, 210–221.

Li, Y.G., Vidale, J.E. & Aki, K., 1997b. San Jacinto fault-zone guided waves: a discrimination for recently active fault strands near Anza, California, *J. Geophys. Res.*, **102** 11,689–11,701.

Li, Y.G., Leary, P., Aki, K. & Malin, P.E., 1990. Seismic trapped modes in the Oroville and San Andreas fault zones, *Science*, **249**, 763–766, 1990.

Li, Y.G., Aki, K., Adams, D., Hasemi, A. & Lee, W.H.K., 1994. Seismic guided waves trapped in the fault zone of the Landers, California, earthquake of 1992, *J. Geophys. Res.*, **99**, 11,705–11,722.

Liu, Y., Teng, T.L. & Ben-Zion, Y., 2004. Systematic analysis of shear wave splitting in the aftershock region of the 1999 Chi-Chi earthquake: Evidence for shallow anisotropic structure and lack of systematic temporal variations, *Bull. Seism. Soc. Am.*, **94**, 2330–2347.

Liu, Y., Teng, T.L. & Ben-Zion, Y., 2005. Near-surface seismic anisotropy, attenuation and dispersion in the aftershock region of the 1999 Chi-Chi earthquake, *Geophys. J. Int.*, **160**(2), 695–706.

McGuire, J. & Ben-Zion, Y., 2005. High-resolution imaging of the Bear Valley section of the San Andreas Fault at seismogenic depths with fault-zone head waves and relocated seismicity, *Geophys. J. Int.*, **163**, 152–164, doi:10.1111/j.1365-246X.2005.02703.x.

Marra, F., Azzara, R., Bellucci, F., Caserta, A., Cultrera, G., Mele, G., Palombo, B., Rovelli, A. & Boschi, E., 2000. Large amplification of ground motion at rock sites within a fault zone in Nocera Umbra (Central Italy), *J. Seis.*, **4** 534–554.

Michael, A.J. & Ben-Zion, Y., 1998. Inverting fault zone head trapped waves with genetic algorithm, *EOS, Trans. Am. Geophys. Un.*, **81**, F1145.

Peng, Z., Ben-Zion, Y., Zhu, L. & Michael, A.J., 2003. Inference of a shallow fault zone layer in the rupture zone of the 1992 Landers, California earthquake fro locations of events generating trapped waves and travel time analysis, *Geophys. J. Int.*, **155**, 1021–1041.

Peng, Z. & Ben-Zion, Y., 2005. Spatio-temporal variations of crustal anisotropy from similar events in aftershocks of the 1999 M7.4 zmit and M7.1 Düzce, Turkey, earthquake sequences, *Geophys. J. Int.*, **160**(3), 1027–1043, doi:10.1111/j.1365-246X.2005.02569.x.

Peng, Z. & Ben-Zion, Y., 2006. Temporal changes of shallow seismic velocity around the Karadere-Duzce branch of the north Anatolian fault and strong ground motion, *Pure Appl. Geophys.*, **163**, 567–599, doi:10.1007/s00024-005-0034-6.

Rovelli, A., Caserta, A., Marra, F. & Ruggiero, V., 2002. Can seismic waves be trapped inside an inactive fault zone? The case study of Nocera Umbra, central Italy, *Bull. Seis. Soc. Am.*, **92**, 2217–2232.

Rubin, A.M. & Gillard, D., 2000, Aftershock asymmetry/rupture directivity among central San Andreas fault micro earthquakes, *J. Geophys. Res.*, **105**, 19 095–19 110.

Rubin, A.M. & Ampuero, J.P., 2007. Aftershock asymmetry on a bimaterial interface, *J. Geophys. Res.*, in press.

Scott, J.S., Masters, T.G. & Vernon, F.L., 1994. 3-D velocity structure of the San Jacinto fault zone near Anza, California – I. *P* waves, *Geophys. J. Int.*, **119**, 611–626.

Shi, Z. & Ben-Zion, Y., 2006. Dynamic rupture on a bimaterial interface governed by slip-weakening friction, *Geophys. J. Int.*, **165**, doi:10.1111/j.1365-246X.2006.02853.x.

Thurber, C., Roecker, S., Ellsworth, W., Chen, Y., Lutter, W. & Sessions, R., 1997. Two-dimensional seismic image of the San Andreas fault in the northern Gabilan range, central California: evidence for fluids in the fault zone, *Geophys. Res. Lett.*, **24**, 1591–1594.

Waldhauser, F. & Ellsworth, W., 2000. A double-difference earthquake location algorithm: method and application to the northern Hayward Fault, *Bull. Seism. Soc Am.*, **90**, 1330–1368.

Weertman, J., 1980. Unstable slippage across a fault that separates elastic media of different elastic constants, *J. Geophys. Res.*, **85**, 1455–1461.